



Enhanced high-temperature thermoelectric properties of Ce- and Dy-doped ZnO for power generation



K. Park^{a,*}, H.K. Hwang^a, J.W. Seo^a, W.-S. Seo^b

^a Faculty of Nanotechnology and Advanced Materials Engineering, Sejong University, Seoul 143-747, Republic of Korea

^b Korea Institute of Ceramic Engineering and Technology, Seoul 153-023, Republic of Korea

ARTICLE INFO

Article history:

Received 22 August 2012

Received in revised form

4 February 2013

Accepted 11 March 2013

Available online 12 April 2013

Keywords:

ZnO

Thermoelectric materials

Sintering

Electrical properties

Ceramics

ABSTRACT

The incorporation of CeO₂ and Dy₂O₃ to ZnO leads to a marked increase in the electrical conductivity. The absolute values of the Seebeck coefficients of Zn_{1-x}Ce_xO and Zn_{1-x}Dy_xO increase with CeO₂ and Dy₂O₃ contents up to $x = 0.003$ and 0.005 , respectively, and then decrease with further increases of their concentrations. The highest power factor ($4.46 \times 10^{-4} \text{ Wm}^{-1} \text{ K}^{-2}$ at 800°C) is attained for Zn_{0.995}Dy_{0.005}O. The power factor is approximately 56 times larger than that of ZnO ($0.08 \times 10^{-4} \text{ Wm}^{-1} \text{ K}^{-2}$ at 800°C). The introduction of a small amount of Dy₂O₃ is highly effective for improving the thermoelectric properties of ZnO.

© 2013 Elsevier Ltd. All rights reserved.

1. Introduction

In order to reduce ozone depletion, greenhouse gas emissions, and fossil fuel usage in our surroundings, thermoelectric power generation technology has attracted considerable attention and has been studied extensively [1]. Currently, there is a large amount of waste heat, especially in the fields of power plants, automobiles, incinerators, and factories. Thermoelectric devices directly convert waste heat into electricity via the Seebeck effect. In thermoelectric devices, a temperature difference drives electron charge carriers from hot to cold junctions, causing an electric current to flow in the circuit. Thermoelectric energy conversion would be fairly suited for waste heat recovery or power generation from a cogeneration process [2–6]. Thermoelectric devices do not have moving components, and are compact, quiet, highly reliable, and environmentally friendly [3,7–9]. Due to these merits, thermoelectricity to harvest waste heat has been systematically investigated in many fields, including military, aerospace, instrument, and industry [10–12]. The primary problem of current

thermoelectric power generation is the relatively low heat-to-electricity conversion efficiency, which consequently, needs to be improved.

Thermoelectric materials are solid-state energy converters whose combination of thermal and electrical properties endows them with heat-to-electricity conversion [1,13]. The performance of thermoelectric materials can be expressed by the figure-of-merit (Z) as follows [14–16]: $Z = \sigma\alpha^2/\kappa$, where σ , α , and κ are the electrical conductivity, Seebeck coefficient, and thermal conductivity, respectively. The electrical properties are determined by the power factor (P) defined as [14]: $P = \sigma\alpha^2$. To be a good thermoelectric material, it is essential to have a large power factor and a low thermal conductivity. Maximizing Z is extremely difficult because generally optimizing one physical parameter adversely affects another. For example, as the Seebeck coefficient increases so does the electrical resistivity and as the electrical conductivity increases so does the thermal conductivity.

Conventional thermoelectric materials, such as Bi₂Te₃, FeSi₂, PbTe, and SiGe, suffer from high toxicity and low thermal stability, whereas ceramics is comprehensively recognized as good thermoelectric, having high thermal stability even at elevated temperatures, low production costs, and no deterioration of their performance due to oxidation [17]. In particular, ZnO is a promising thermoelectric material due to its high figure-of-merit Z at high

* Corresponding author. Tel.: +82 2 3408 3777; fax: +82 2 3408 4342.
E-mail address: kspark@sejong.ac.kr (K. Park).

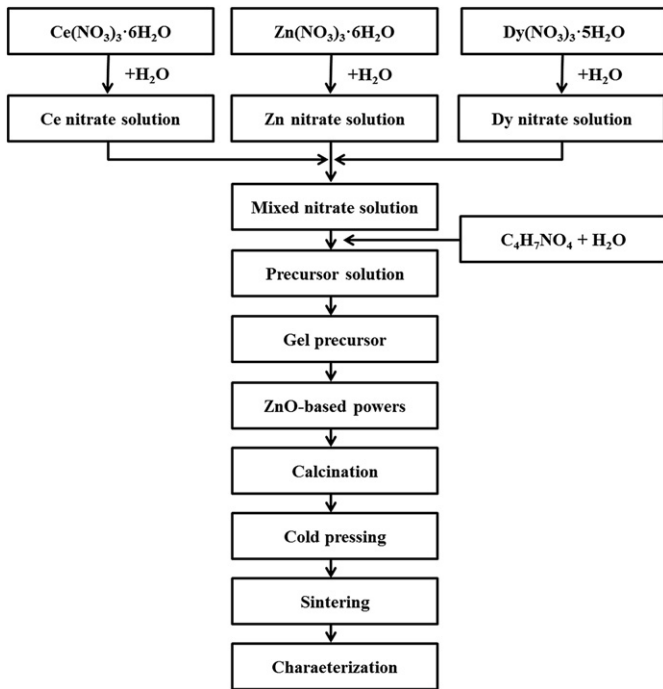


Fig. 1. A schematic diagram showing the experimental procedures of the $\text{Zn}_{1-x}\text{R}_x\text{O}$ samples.

temperatures [18]. However, the obtained results are still insufficient for the practical application of thermoelectric power generation. It is known that an effective way to enhance thermoelectric properties is to introduce a small amount of dopant [19,20]. Therefore, in the present study, we attempt to improve the thermoelectric properties of ZnO with the introduction of a small amount of CeO_2 and Dy_2O_3 .

2. Experimental

Nano-sized $\text{Zn}_{1-x}\text{R}_x\text{O}$ (R : Ce and Dy; $0 \leq x \leq 0.01$) powders were synthesized by the combustion synthesis process using $\text{Zn}(\text{NO}_3)_2 \cdot 6\text{H}_2\text{O}$, $\text{Ce}(\text{NO}_3)_3 \cdot 6\text{H}_2\text{O}$, and $\text{Dy}(\text{NO}_3)_3 \cdot 5\text{H}_2\text{O}$ as the oxidizers and aspartic acid ($\text{C}_4\text{H}_7\text{NO}_4$) as the fuel. The metal nitrates were dissolved separately in distilled water to prepare homogeneous solutions. The aspartic acid was dissolved in the solutions to prepare a transparent aqueous solution. The molar ratio of the metal nitrates to aspartic acid was adjusted to 1:1. The obtained solution was slowly heated on a hot plate at 300°C until a highly viscous gel precursor was obtained. Subsequently, the gel precursor was auto-ignited with the rapid evolution of a large volume of gases to produce voluminous powders.

The size and morphological characteristics of the synthesized powders were investigated with a field emission scanning electron microscope (FE-SEM; Hitachi S4700) and a transmission electron

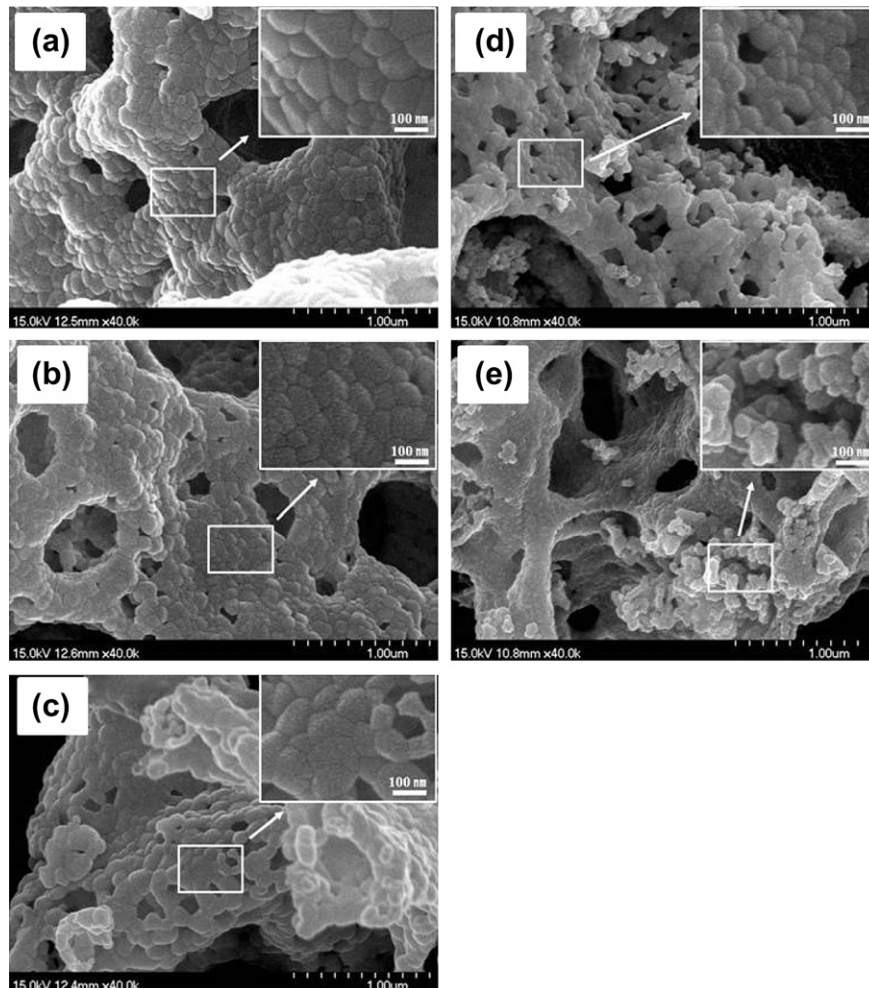


Fig. 2. FE-SEM images of the synthesized $\text{Zn}_{1-x}\text{Ce}_x\text{O}$ with $x =$ (a) 0, (b) 0.005, and (c) 0.01 and of the synthesized $\text{Zn}_{1-x}\text{Dy}_x\text{O}$ with $x =$ (d) 0.005 and (e) 0.01.

microscope (TEM; JEM-2100F, JEOL) operating at 200 kV. The resultant powders were calcined at 950 °C for 5 h. Subsequently, the calcined powders were cold-pressed under 150 MPa to prepare green pellets. The pellets were heated at 1350 °C for 10 h in air and then furnace cooled. The crystal structure of the calcined powders and sintered pellets was analyzed with an X-ray diffractometer (XRD; Rigaku DMAX 2500) using Cu K α radiation at 40 kV and 100 mA. Thermal etching at 1300 °C for 30 min in air was performed after polishing the sintered pellets. The microstructure of the sintered pellets was investigated with a field emission scanning electron microscope (FE-SEM, Hitachi S-4700). The density of the sintered pellets was measured by the Archimedes method. Thermoelectric properties were measured in temperature range of 500–800 °C. Electrical conductivity was measured by the direct current (dc) four-probe method. The temperature difference (ΔT) between the two ends in the samples was controlled at 4–6 °C to measure the Seebeck coefficient. The thermoelectric voltage (ΔE) measured as a function of the temperature difference (ΔT) produced a straight line. A schematic diagram showing the experimental procedures of the $\text{Zn}_{1-x}\text{R}_x\text{O}$ samples is shown in Fig. 1.

3. Results and discussion

Fig. 2 shows FE-SEM images from the synthesized $\text{Zn}_{1-x}\text{Ce}_x\text{O}$ and $\text{Zn}_{1-x}\text{Dy}_x\text{O}$ powders. The FE-SEM images exhibit sponge-like agglomerated powders due to the liberation of a large amount of gas during the combustion of gels [21]. In order to investigate the size and morphology of the synthesized $\text{Zn}_{1-x}\text{R}_x\text{O}$ (R: Ce and Dy) powders, TEM bright field images are obtained. The synthesized $\text{Zn}_{1-x}\text{R}_x\text{O}$ powders show a spherical morphology and ultra-fine size. The TEM bright field images of the synthesized $\text{Zn}_{1-x}\text{R}_x\text{O}$ powders are shown in Fig. 3.

Fig. 4(a) and (b) show the XRD patterns of the calcined $\text{Zn}_{1-x}\text{Ce}_x\text{O}$ and $\text{Zn}_{1-x}\text{Dy}_x\text{O}$ ($0 \leq x \leq 0.01$) powders, respectively. The $\text{Zn}_{1-x}\text{Ce}_x\text{O}$ ($0.001 \leq x \leq 0.01$) powders consist of the $\text{Zn}_{1-x}\text{Ce}_x\text{O}$ phase with a wurtzite structure and the CeO_2 phase with a cubic structure [22–24], and the $\text{Zn}_{1-x}\text{Dy}_x\text{O}$ ($0.001 \leq x \leq 0.01$) powders consist of the $\text{Zn}_{1-x}\text{Dy}_x\text{O}$ phase and the Dy_2O_3 phase with a cubic structure [25]. The general trend is for the intensity of CeO_2 and Dy_2O_3 peaks to increase with an increase in their contents. The added CeO_2 and Dy_2O_3 ($0.001 \leq x \leq 0.01$) are not completely dissolved in the ZnO crystal lattice due to its low solubility.

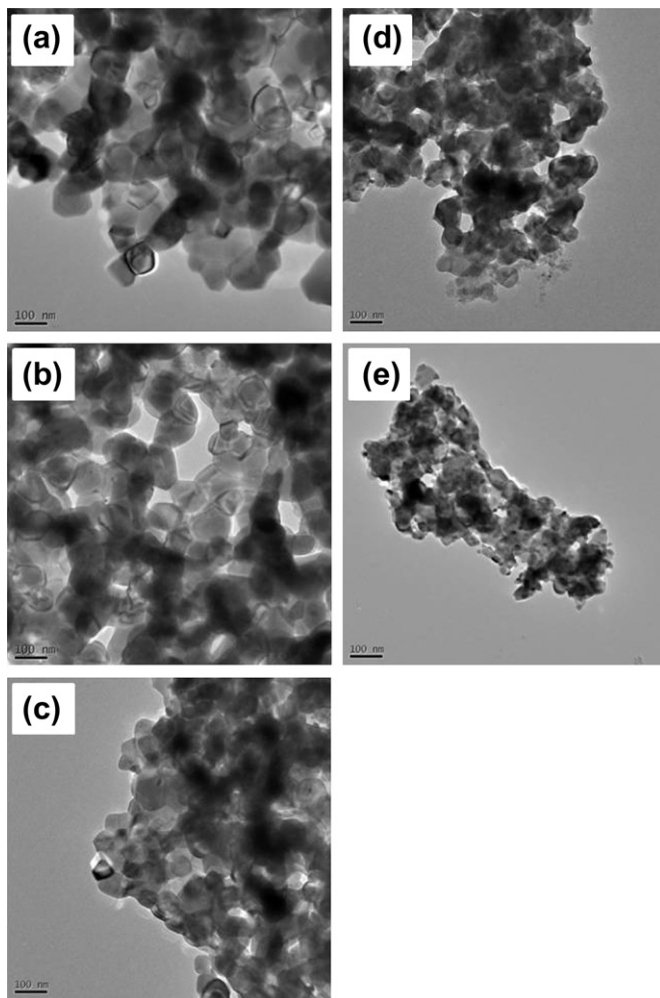


Fig. 3. TEM bright field images of the synthesized $\text{Zn}_{1-x}\text{Ce}_x\text{O}$ with $x =$ (a) 0, (b) 0.005, and (c) 0.01 and of the synthesized $\text{Zn}_{1-x}\text{Dy}_x\text{O}$ with $x =$ (d) 0.005 and (e) 0.01.

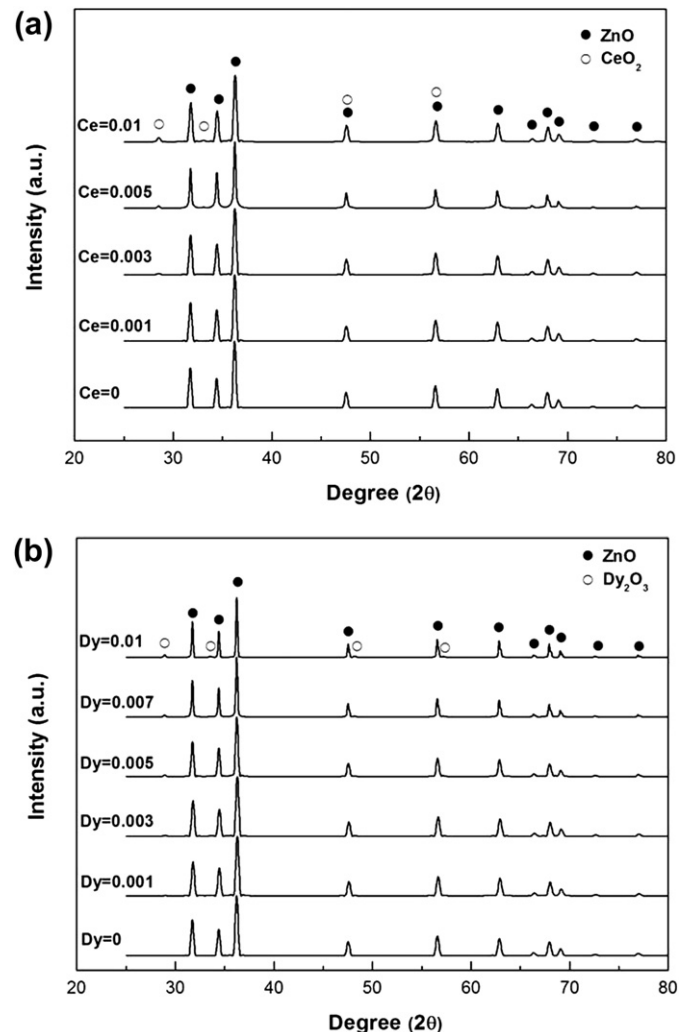


Fig. 4. XRD patterns of the calcined (a) $\text{Zn}_{1-x}\text{Ce}_x\text{O}$ and (b) $\text{Zn}_{1-x}\text{Dy}_x\text{O}$ ($0 \leq x \leq 0.01$) powders.

The XRD peaks are sharpened after sintering at 1350 °C, as shown in Fig. 5, indicating an increased crystallite size and improved crystallinity. In addition to the $\text{Zn}_{1-x}\text{R}_x\text{O}$ phase, the sintered $\text{Zn}_{1-x}\text{Ce}_x\text{O}$ and $\text{Zn}_{1-x}\text{Dy}_x\text{O}$ contain a small amount of the CeO_2 and Dy_2O_3 phases, respectively. This means that the sintered $\text{Zn}_{1-x}\text{R}_x\text{O}$ has the same crystal structure as the calcined powders of the same composition. The presence of CeO_2 and Dy_2O_3 in the sintered samples is further confirmed by the SEI and elemental map studies below.

Fig. 6 shows FE-SEM images from the surfaces of the thermal-etched $\text{Zn}_{1-x}\text{R}_x\text{O}$ ($0 \leq x \leq 0.01$). The grain size of $\text{Zn}_{1-x}\text{R}_x\text{O}$ increases with the small addition of R, i.e., 0.003 and 0.005 for CeO_2 and Dy_2O_3 , respectively, because the added R increases the activity of ZnO by means of the distortion of the ZnO lattice [26]. In contrast, the grain size for high R content, i.e., ≥ 0.005 and ≥ 0.007 for CeO_2 and Dy_2O_3 , respectively, gradually decreases by further increasing their contents. This is attributed to the pinning effect caused by the CeO_2 and Dy_2O_3 phases as well as to the dragging effect between the grain boundaries and the phases, resulting in reduced mobility of the grain boundaries [27,28]. The density of the $\text{Zn}_{1-x}\text{Ce}_x\text{O}$ and $\text{Zn}_{1-x}\text{Dy}_x\text{O}$ is of the same trend as the grain size. Most pores exist at the grain boundaries, and some also remain within individual grains. The grain size and porosity of all the fabricated $\text{Zn}_{1-x}\text{Ce}_x\text{O}$ and $\text{Zn}_{1-x}\text{Dy}_x\text{O}$ are given in Table 1. In

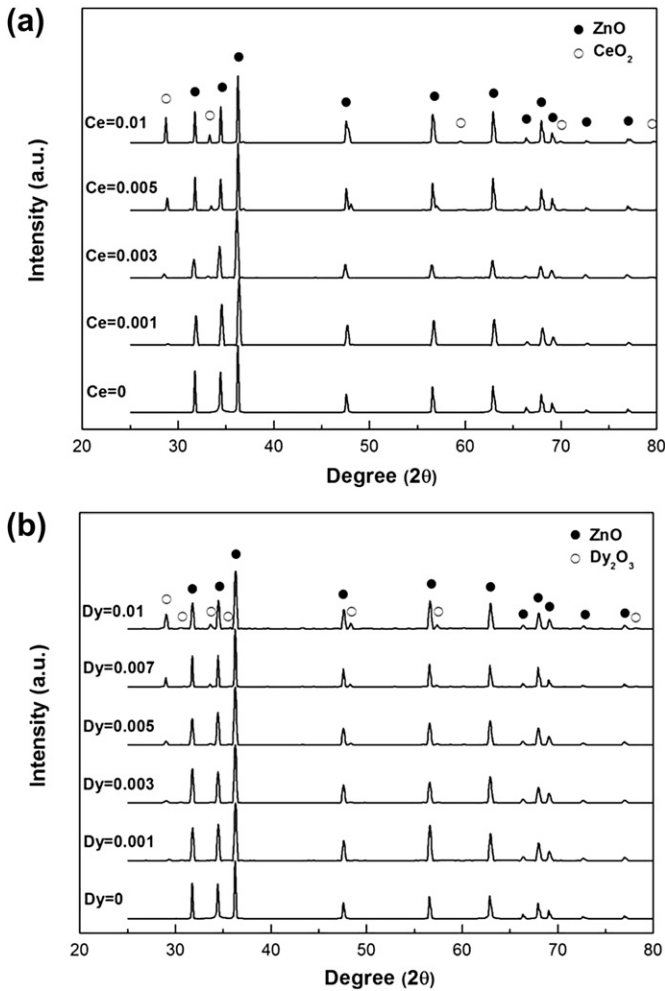


Fig. 5. XRD patterns of the sintered (a) $\text{Zn}_{1-x}\text{Ce}_x\text{O}$ and (b) $\text{Zn}_{1-x}\text{Dy}_x\text{O}$ ($0 \leq x \leq 0.01$).

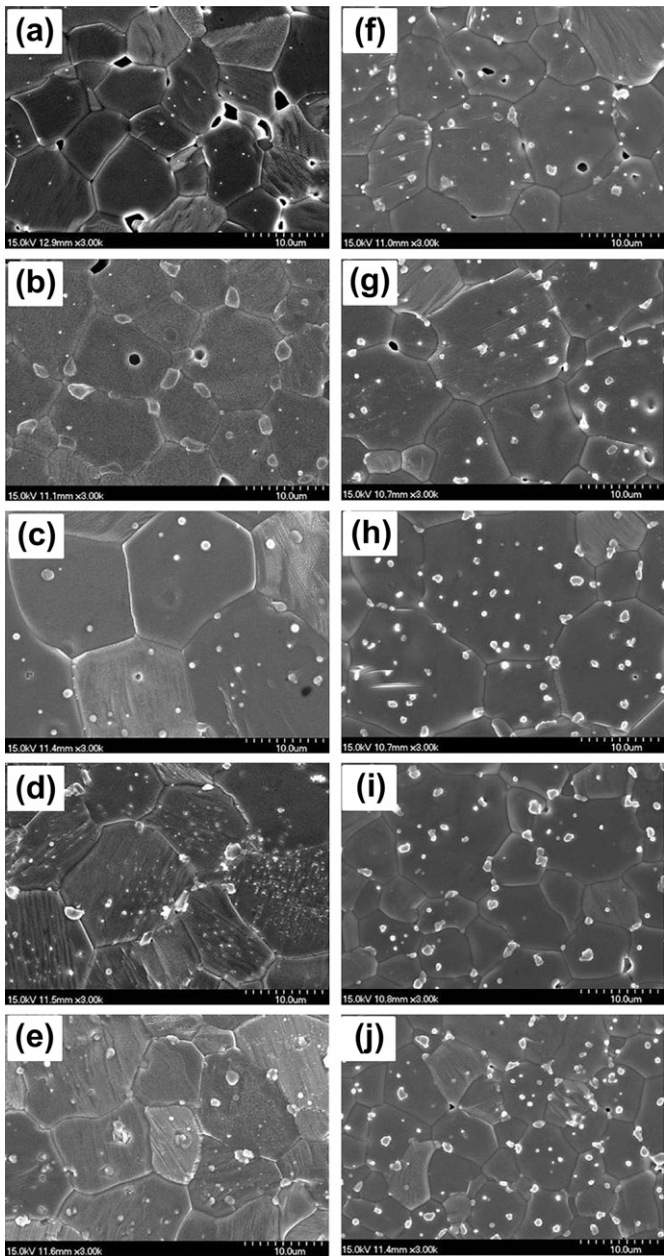


Fig. 6. FE-SEM images from the surfaces of the thermal-etched $\text{Zn}_{1-x}\text{Ce}_x\text{O}$ with $x =$ (a) 0, (b) 0.001, (c) 0.003, (d) 0.005, and (e) 0.01 and of the thermal-etched $\text{Zn}_{1-x}\text{Dy}_x\text{O}$ with $x =$ (f) 0.001, (g) 0.003, (h) 0.005, (i) 0.007, and (j) 0.01.

Table 1
The grain size and porosity of all the fabricated $\text{Zn}_{1-x}\text{Ce}_x\text{O}$ and $\text{Zn}_{1-x}\text{Dy}_x\text{O}$ ($0 \leq x \leq 0.01$).

		Grain size (μm)	Porosity (%)
$\text{Zn}_{1-x}\text{Ce}_x\text{O}$	0	8.2	12.5
	0.001	8.5	6.6
	0.003	13.9	4.8
	0.005	12.1	5.1
	0.01	10.2	5.5
$\text{Zn}_{1-x}\text{Dy}_x\text{O}$	0.001	9.4	9.1
	0.003	12.8	4.8
	0.005	14.6	4.1
	0.007	10.1	4.4
	0.01	6.5	5.3

order to identify the distribution of constituent elements in the sintered $\text{Zn}_{1-x}\text{Ce}_x\text{O}$ and $\text{Zn}_{1-x}\text{Dy}_x\text{O}$, SEI and elemental mapping are obtained. Fig. 7(a) and (b) show the SEI and elemental mapping of $\text{Zn}_{0.99}\text{Ce}_{0.01}\text{O}$ and $\text{Zn}_{0.99}\text{Dy}_{0.01}\text{O}$, respectively. In the as-sintered samples, Zn and O distributions are relatively homogeneous, while Ce and Dy distributions are heterogeneous, suggesting the formation of CeO_2 and Dy_2O_3 at the grain boundaries and in the innergrain.

The electrical conductivities (σ) of $\text{Zn}_{1-x}\text{Ce}_x\text{O}$ and $\text{Zn}_{1-x}\text{Dy}_x\text{O}$ ($0 \leq x \leq 0.01$) as a function of temperature are shown in Fig. 8(a) and (b), respectively. The electrical conductivity slightly increases

with increasing temperature, indicating semiconducting behavior. In addition, the incorporation of CeO_2 and Dy_2O_3 to ZnO leads to a marked increase in the electrical conductivity. This is caused by the fact that the substitution of Ce^{4+} and Dy^{3+} for Zn^{2+} may increase the electron concentration of the system to compensate for the electric charge balance. The electrical conductivities at 800 °C for the $\text{Zn}_{1-x}\text{Ce}_x\text{O}$ and $\text{Zn}_{1-x}\text{Dy}_x\text{O}$ are in the ranges of 20.4–71.9 $\Omega^{-1}\text{cm}^{-1}$, and 20.4 to 97.8 $\Omega^{-1}\text{cm}^{-1}$, respectively.

Fig. 9(a) and (b) show the Seebeck coefficients (α) of $\text{Zn}_{1-x}\text{Ce}_x\text{O}$ and $\text{Zn}_{1-x}\text{Dy}_x\text{O}$ ($0 \leq x \leq 0.01$), respectively. The Seebeck coefficient

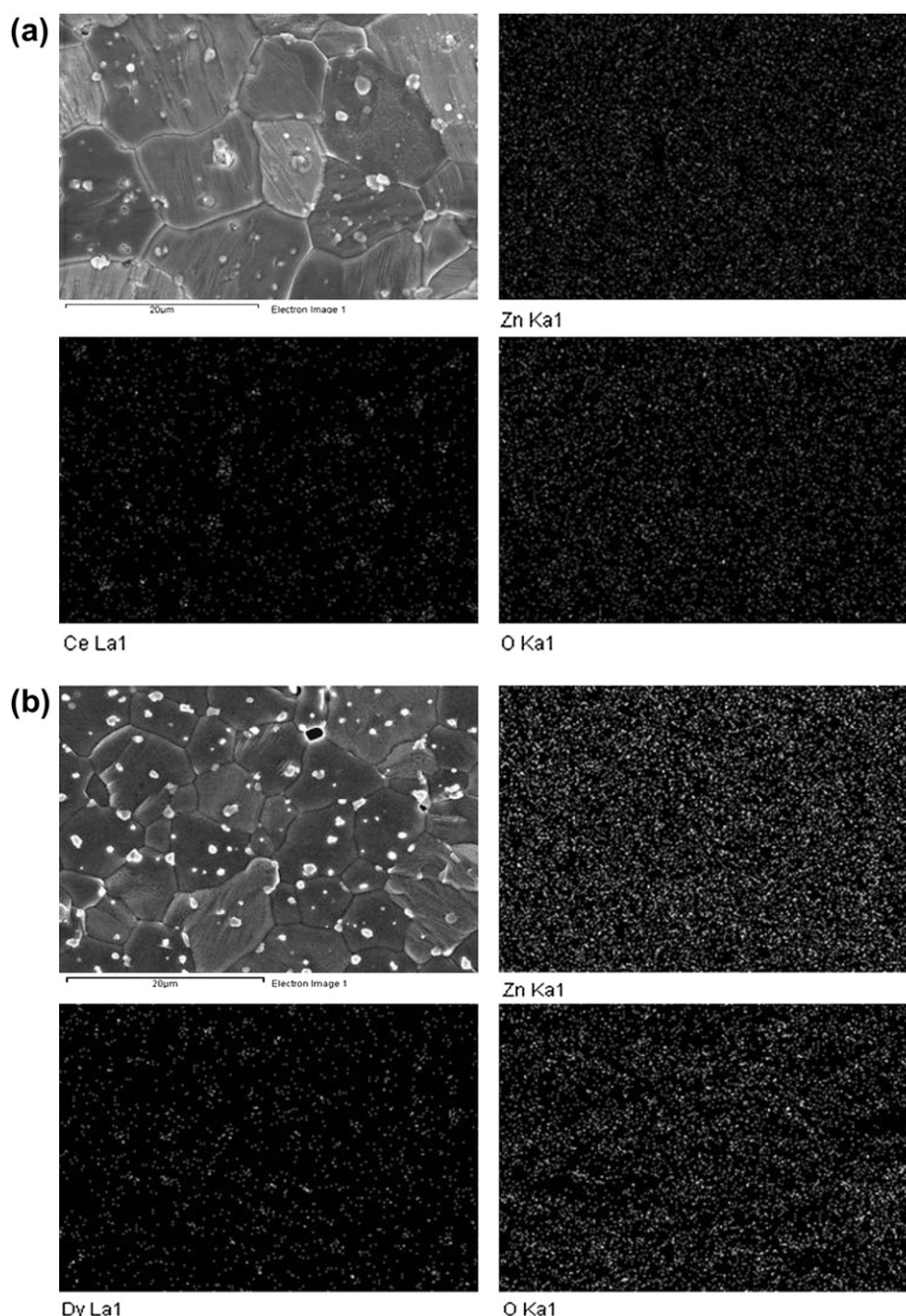


Fig. 7. SEI and elemental mapping of the (a) $\text{Zn}_{0.99}\text{Ce}_{0.01}\text{O}$ and (b) $\text{Zn}_{0.99}\text{Dy}_{0.01}\text{O}$.

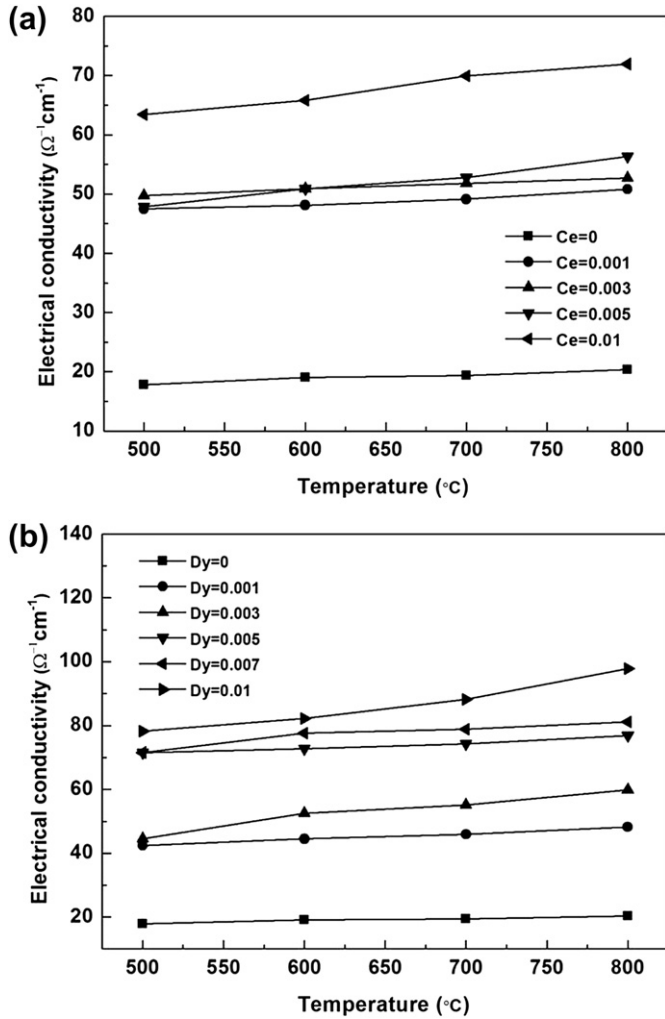


Fig. 8. Electrical conductivity of the (a) Zn_{1-x}Ce_xO and (b) Zn_{1-x}Dy_xO ($0 \leq x \leq 0.01$).

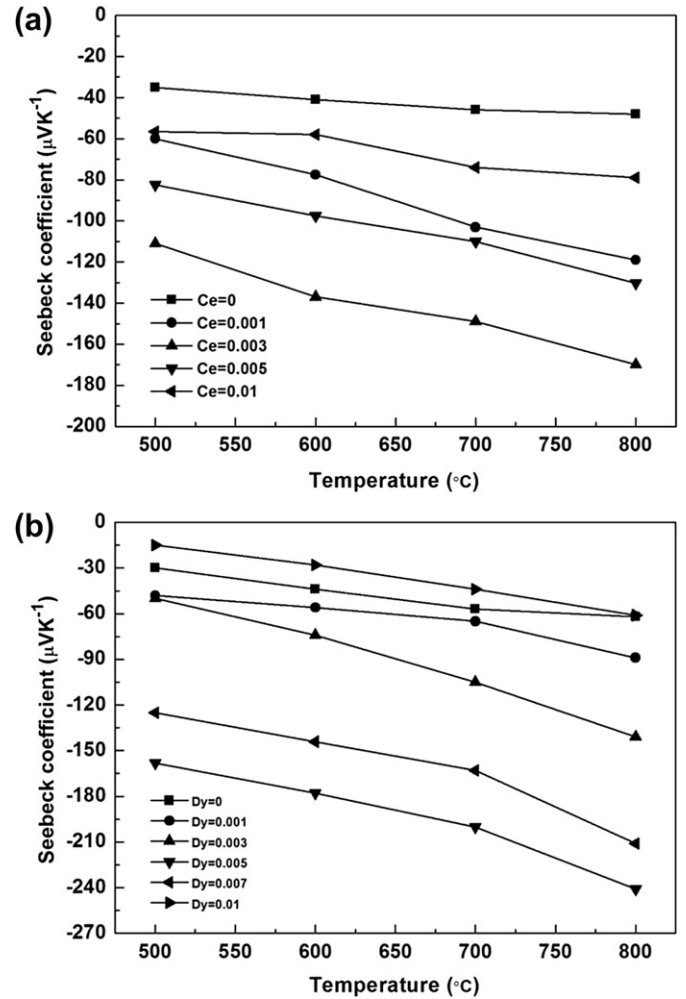


Fig. 9. Seebeck coefficient of the (a) Zn_{1-x}Ce_xO and (b) Zn_{1-x}Dy_xO ($0 \leq x \leq 0.01$).

(α) is calculated with the following equation: $\alpha = \Delta E / \Delta T$, where ΔE is the thermoelectric voltage and ΔT is the temperature difference between the two ends of the sample [29]. The sign of the Seebeck coefficient is negative over the whole temperature range for all the samples, indicating that the major conductivity carriers are electrons. The absolute values of the Seebeck coefficients at 800 °C for the Zn_{1-x}Ce_xO and Zn_{1-x}Dy_xO are in the ranges of 48–170 μVK^{-1} and 48 to 241 μVK^{-1} , respectively. The absolute value of the Seebeck coefficient for Zn_{1-x}Ce_xO and Zn_{1-x}Dy_xO ($0.001 \leq x \leq 0.01$) is much larger than that of ZnO. The absolute values of the Seebeck coefficients of the Zn_{1-x}Ce_xO and Zn_{1-x}Dy_xO first increase with increasing the CeO₂ and Dy₂O₃ contents, reaching a maximum at $x = 0.003$ and 0.005 , respectively, and then decrease with further increases of their contents. It is also important to note that both the electrical conductivity and the absolute values of the Seebeck coefficients of the Zn_{1-x}Ce_xO and Zn_{1-x}Dy_xO increase with increasing the CeO₂ and Dy₂O₃ contents up to $x = 0.003$ and 0.005 , respectively. The absolute values of the Seebeck coefficients of Zn_{0.997}Dy_{0.003}O and Zn_{0.995}Dy_{0.005}O are as high as 170 and 241 μVK^{-1} , respectively. The temperature dependence of the electrical conductivity and the Seebeck coefficient observed in this

study is unusual. In general, by increasing the electrical conductivity, the Seebeck coefficient decreases [30]. The reason for this unusual occurrence is unclear at present, requiring further experiments in the future.

The temperature dependences of the power factors ($\sigma\alpha^2$), calculated from the data in Figs. 8 and 9, for Zn_{1-x}Ce_xO and Zn_{1-x}Dy_xO ($0 \leq x \leq 0.01$) are plotted in Fig. 10(a) and (b), respectively. As expected, the power factor of Zn_{1-x}Ce_xO and Zn_{1-x}Dy_xO increases up to 800 °C. The power factor of the CeO₂- and Dy₂O₃-doped samples is much greater than that of ZnO. The addition of CeO₂ and Dy₂O₃ up to $x = 0.003$ and 0.005 , respectively, results in a higher power factor at high temperatures because it simultaneously enhances the electrical conductivity and the absolute value of the Seebeck coefficient. The power factor of Zn_{0.995}Dy_{0.005}O at 800 °C is as high as $4.46 \times 10^{-4} \text{ Wm}^{-1} \text{ K}^{-2}$, which is about 56 times larger than that given by ZnO at 800 °C ($0.08 \times 10^{-4} \text{ Wm}^{-1} \text{ K}^{-2}$). This means that the doped Dy₂O₃ is highly effective for improving the thermoelectric properties of ZnO. The value of the power factor for the Zn_{1-x}Ce_xO and Zn_{1-x}Dy_xO still increases toward higher temperatures, implying high performance and thermal stability at high temperatures.

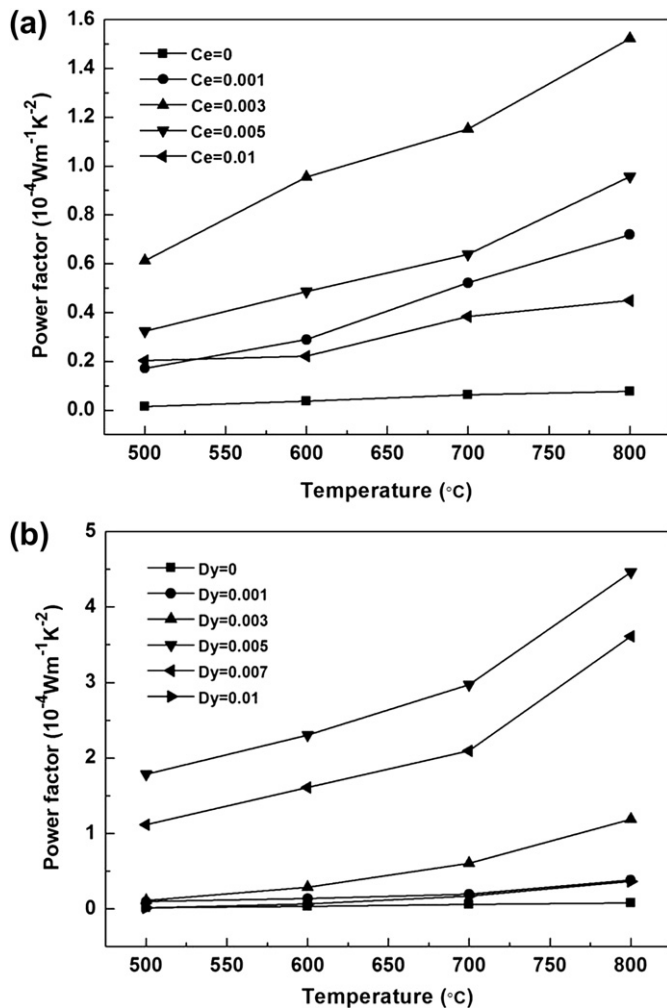


Fig. 10. Power factor of the (a) $\text{Zn}_{1-x}\text{Ce}_x\text{O}$ and (b) $\text{Zn}_{1-x}\text{Dy}_x\text{O}$ ($0 \leq x \leq 0.01$).

4. Conclusions

The sintered $\text{Zn}_{1-x}\text{Ce}_x\text{O}$ ($0.001 \leq x \leq 0.01$) contains the $\text{Zn}_{1-x}\text{Ce}_x\text{O}$ phase and the secondary CeO_2 phase, while the sintered $\text{Zn}_{1-x}\text{Dy}_x\text{O}$ ($0.001 \leq x \leq 0.01$) contains the $\text{Zn}_{1-x}\text{Dy}_x\text{O}$ phase and the secondary Dy_2O_3 phase. The intensities of the CeO_2 and Dy_2O_3 peaks increase with increases in the CeO_2 and Dy_2O_3 contents, respectively. The electrical conductivities of $\text{Zn}_{1-x}\text{Ce}_x\text{O}$ and $\text{Zn}_{1-x}\text{Dy}_x\text{O}$ ($0 \leq x \leq 0.01$) increase with increasing CeO_2 and Dy_2O_3 contents. The absolute values of the Seebeck coefficients of the $\text{Zn}_{1-x}\text{Ce}_x\text{O}$ and $\text{Zn}_{1-x}\text{Dy}_x\text{O}$ first increase with increasing the CeO_2 and Dy_2O_3 contents up to $x = 0.003$ and 0.005 , respectively, and then decrease with further increasing their contents. Among the fabricated samples, the maximal power factor ($4.46 \times 10^{-4} \text{ Wm}^{-1} \text{ K}^{-2}$ at 800°C) is attained for the $\text{Zn}_{0.995}\text{Dy}_{0.005}\text{O}$, which is approximately 56 times higher than that for ZnO ($0.08 \times 10^{-4} \text{ Wm}^{-1} \text{ K}^{-2}$ at 800°C). It is therefore believed that a small amount of Dy_2O_3 is fairly effective in achieving a high power factor.

Acknowledgment

This research was supported by Basic Science Research Program through the National Research Foundation of Korea (NRF) funded

by the Ministry of Education, Science and Technology (2012R1A1A2009194).

References

- [1] Bell LE. Cooling, heating, generating power, and recovering waste heat with thermoelectric systems. *Science* 2008;321:1457–61.
- [2] Qiu K, Hayden ACS. Development of a novel cascading TPV and TE power generation system. *Applied Energy* 2012;91:304–8.
- [3] Sahin AZ, Yilbas BS, Shuja SZ, Momin O. Investigation into topping cycle: thermal efficiency with and without presence of thermoelectric generator. *Energy* 2011;36:4048–54.
- [4] Hsiao YY, Chang WC, Chen SL. A mathematic model of thermoelectric module with applications on waste heat recovery from automobile engine. *Energy* 2010;35:1447–54.
- [5] Walker ME, Safari I, Theragowda RB, Hsieh MK, Abbasian, Arastoopour H, et al. Economic impact of condenser fouling in existing thermoelectric power plants. *Energy* 2012;44:429–37.
- [6] Champier D, Bedecarrats JP, Rivaletto M, Strub F. Thermoelectric power generation from biomass cook stoves. *Energy* 2010;35:935–42.
- [7] Gou X, Xiao H, Yang S. Modeling, experimental study and optimization on low-temperature waste heat thermoelectric generator system. *Applied Energy* 2010;87(10):3131–6.
- [8] Wang CC, Hung CI, Chen WH. Design of heat sink for improving the performance of thermoelectric generator using two-stage optimization. *Energy* 2012;39:236–45.
- [9] Chen WH, Liao CY, Hung CI, Huang WL. Experimental study on thermoelectric modules for power generation at various operating conditions. *Energy* 2012;45:874–81.
- [10] Chen L, Li J, Sun F, Wu C. Performance optimization of a two-stage semiconductor thermoelectric-generator. *Applied Energy* 2005;82(4):300–12.
- [11] Hsu CT, Huang GY, Chu HS, Yu B, Yao DJ. Experiments and simulations on low-temperature waste heat harvesting system by thermoelectric power generators. *Applied Energy* 2011;88(4):1291–7.
- [12] Cheng TC, Cheng CH, Huang ZZ, Liao GC. Development of an energy-saving module via combination of solar cells and thermoelectric coolers for green building applications. *Energy* 2011;36:133–40.
- [13] Champier D, Bédécarrats JP, Kouskou T, Rivaletto M, Strub F, Pignolet P. Study of a TE (thermoelectric) generator incorporated in a multifunction wood stove. *Energy* 2011;36:1518–26.
- [14] Bhandari CM, Rowe DM. Optimization of carrier concentration, CRC handbook of thermoelectrics. Boca Raton: CRC Press; 1995.
- [15] Yilbas BS, Sahin AZ. Thermoelectric device and optimum external load parameter and slenderness ratio. *Energy* 2010;35:5380–4.
- [16] Wang XD, Huang YX, Cheng CH, Lin DTW, Kang CH. A three-dimensional numerical modeling of thermoelectric device with consideration of coupling of temperature field and electric potential field. *Energy* 2012;47:488–97.
- [17] Weidenkaff A, Robert R, Aguirre M, Bocher L, Lippert T, Canulescu S. Development of thermoelectric oxides for renewable energy conversion technologies. *Renewable Energy* 2008;33:342–7.
- [18] Ohtaki M, Tsubota T, Eguchi K, Arai H. High-temperature thermoelectric properties of $(\text{Zn}_{1-x}\text{Al}_x)\text{O}$. *Journal of Applied Physics* 1996;79:1816–8.
- [19] Park K, Ko KY, Seong JK, Nahm S. Microstructure and high-temperature thermoelectric properties of polycrystalline $\text{CuAl}_{1-x}\text{Mg}_x\text{O}_2$. *Journal of the European Ceramic Society* 2007;27:3735–8.
- [20] Nam SW, Lim YS, Choi SM, Seo WS, Park K. Thermoelectric properties of nanocrystalline $\text{Ca}_{3-x}\text{Cu}_x\text{Co}_4\text{O}_9$ ($0 \leq x \leq 0.32$) for power generation. *Journal of Nanoscience and Nanotechnology* 2011;11:1734–7.
- [21] Bansal NP, Zhong Z. Combustion synthesis of $\text{Sm}_{0.5}\text{Sr}_{0.5}\text{CoO}_{3-x}$ and $\text{La}_{0.5}\text{Sr}_{0.5}\text{CoO}_{3-x}$ nanopowders for solid oxide fuel cell cathodes. *Journal of Power Sources* 2006;158(1):148–53.
- [22] Colder H, Guilmeau E, Harnois C, Marinel S, Retoux R, Savary E. Preparation of Ni-doped ZnO ceramics for thermoelectric applications. *Journal of the European Ceramic Society* 2011;31(15):2957–63.
- [23] Ma N, Li JF, Zhang BP, Lin YH, Ren LR, Chen GF. Microstructure and thermoelectric properties of $\text{Zn}_{1-x}\text{Al}_x\text{O}$ ceramics fabricated by spark plasma sintering. *Journal of Physics and Chemistry of Solids* 2010;71(9):1344–9.
- [24] JCPDS No. 43–1002.
- [25] JCPDS No. 88–2164.
- [26] Zhu BL, Xie CS, Wang WY, Huang KJ, Hu JH. Improvement in gas sensitivity of ZnO thick film to volatile organic compounds (VOCs) by adding TiO_2 . *Materials Letters* 2004;58(5):624–9.
- [27] Bernik S, Daneu N, Rečnik A. Inversion boundary induced grain growth in TiO_2 or Sb_2O_3 doped ZnO-based varistor ceramics. *Journal of the European Ceramics Society* 2004;24:3703–8.
- [28] Cotterill P, Mould PR. Recrystallization and grain growth in metals. 1st ed. New York: John Wiley & Sons; 1976.
- [29] Kubo M, Shinoda M, Furuhashi T, Kitagawa K. Optimization of the incision size and cold-end temperature of a thermoelectric device. *Energy* 2005;30:2156–70.
- [30] Park K, Seong JK, Nahm S. Improvement of thermoelectric properties with the addition of Sb to ZnO. *Journal of Alloys and Compounds* 2008;455:331–5.